Ultra-long bismuth telluride nanoribbons synthesis by lithographically patterned galvanic displacement†

Hyunsung Jung,[a] Youngwoo Rheem,[a] Nicha Chartuprayoon,[a] Jae-Hong Lim,[b] Kyu-Hwan Lee,[b] Bongyoung Yoo,[c] Kun-Jae Lee,[c] Yong-Ho Choa,[c] Peng Wei,[d] Jing Shi[d] and Nosang V. Myung*[a]

Received 29th June 2010, Accepted 6th September 2010
DOI: 10.1039/c0jm02058c

We demonstrated the wafer level batch synthesis and fabrication of single semiconducting thermoelectric nanoribbon based devices by Lithographically Patterned Galvanic Displacement (LPGD). The shape, composition, and dimension of nanoribbons were tailored by adjusting deposition conditions. High resolution TEM images with fast Fourier transform (FFT)-converted selected area electron diffraction (SAED) patterns confirmed the formation of polycrystalline Bi_2Te_3 intermetallic compound with a rhombohedral structure without elemental Te and Bi. The thickness dependent electrical resistivity of Bi_xTe_y nanoribbons shows a classic size effect due to the increase in surface boundary scattering. The as-synthesized nanoribbons were n-type semiconductors with no clear trend between field effect carrier mobility and composition, which might be attributed to the trapped charges at the interface between the channel and dielectric layer. The preliminary results on thermoelectric properties (*i.e.* Seebeck coefficient and power factor) show that the Seebeck coefficient of as-synthesized 0.1 μm thick $Bi_{30}Te_{70}$ nanoribbon is comparable with bulk counterparts, however, the power factor was lower because of poor crystallinity which leads to higher resistivity.

Introduction

One-dimensional (1-D) nanostructures are extremely attractive for many applications including electronics, optoelectronics, data storage, sensors, and thermoelectrics, because they can function as both devices and the wires that access them.[1–10] While many reports have demonstrated the power of nanoengineered materials as high performance low-density devices, the fabrication methods employed are seriously limited in terms of high-density complex nanodevices. 1-D nanostructures are usually synthesized using either the "top-down" or the "bottom-up" approaches. "Top-down" approaches usually utilize planar lithographic techniques to transfer pre-designed patterns to a substrate, which can form complex high density microstructures in well-defined positions on substrates. However, achieving dimensions much less than readily available optical wavelengths often requires slow, expensive, serial processes such as electron-beam, focus ion beam, and scanning-probe lithography.[11,12] "Bottom-up" approaches can mitigate this difficulty by confining the dimension of nanostructures within a scaffold/template.[13] However, bottom-up approaches are limited in the types of templates, and thus wire geometries, that may be produced. In addition, "bottom-up" template synthesized nanowires need post-positioning and assembling to create devices.

The success of nanodevices depends on new nanofabrication methods which can mass produce nanostructures in a cost-effective manner and reproducible position nanostructures between closely spaced microelectrodes. Lithographically Patterned Nanowire Electrodeposition (LPNE) which was reported by Penner *et al.*[14,15] overcomes the obstacles by combining the advantages of "top-down" photolithography and "bottom-up" electrodeposition to synthesize complex high density nanowires to pre-determined locations. They demonstrated the concept by synthesizing noble metallic (*e.g.* Au, Pd, and Pt) and semiconducting PbTe nanowires on comparatively large areas (>1 cm^2), with a high level of dimensional uniformity.

Galvanic displacement reaction is an electrochemical process induced by the difference in electronegativity (*i.e.* redox potential) between materials. Unlike electrodeposition, galvanic displacement does not require electrodes to connect with an external power supply. Thus, more complex shaped nanostructures can be synthesized.

Thermoelectric (TE) energy converters are solid-state devices that can generate electricity by harvesting waste thermal energy, thereby improving the efficiency of a system. The many advantages of TE devices include solid-state operation, zero-emissions, vast scalability, no maintenance and a long operating lifetime. Nonetheless, due to their limited energy conversion efficiencies, thermoelectric devices currently have a rather limited set of applications. However, there is a reinvigorated interest in the field of thermoelectrics by identifying classical and quantum

[a]*Department of Chemical and Environmental Engineering, University of California-Riverside, Riverside, CA 92521, USA. E-mail: myung@engr.ucr.edu; Fax: +1 951 827 5696; Tel: +1 951 827 7710*
[b]*Electrochemical Processing Group, Korea Institute of Materials Science, Changwon-Si, Kyungnam, 641-010, South Korea*
[c]*Division of Materials and Chemical Engineering, Hanyang University, Ansan, 426-791, South Korea*
[d]*Department of Physics and Astronomy, University of California-Riverside, Riverside, CA, 92521, USA*

† Electronic supplementary information (ESI) available: Composition of Bi_xTe_y nanoribbons and deposition rate as a function of the trench depth, SEM images of FIB-milled specimens, AFM images of nanoribbons with different compositions, back gated Bi_xTe_y nanoribbons FET properties and temperature dependence of the resistivity of the annealed Bi_xTe_y nanoribbons. See DOI: 10.1039/c0jm02058c

mechanical size effects, which provide additional ways to enhance energy conversion efficiencies in nanostructured materials including one-dimensional nanostructures, which are predicted to exceed a ZT of 5.[16–18]

Experimental

Highly doped Si (p-type) wafers with atomic layer epitaxially grown SiO_2 (0.3 μm) were used as substrates (Fig. 1a). Nickel and the photoresist layer (S1813 from Rohm and HAAS Electronic Materials, Inc.) were e-beam evaporated and spin-coated, respectively, followed by patterning the photoresist using standard photolithography techniques (Fig. 1b and c). Two different thicknesses (0.025 μm and 0.1 μm) of nickel layers were utilized to demonstrate control over the thickness of the nanoribbons. To ensure the complete removal of the exposed Ni films with smooth undercut profiles, a two step etching process was adopted with chemically etching by a commercial Ni etchant [Type TFB, Transene company Inc.] prior to electrochemically etching to ensure complete removal of the exposed Ni film and produce smooth undercut profiles. The electrochemical etching electrolyte was composed of KCl (0.1 M) and HCl (0.024 M). Although the chemical etch step imposed a slight recess on the Ni nanoband, the trench formation was very uneven and relatively insensitive to time, with nm to <1 μm undercuts after 5 minutes. The first step was necessary to prevent island formation due to the large open areas typical of our custom patterns. While the islands were not completely detrimental to our process they were subject to non-preferential Bi_xTe_y deposition due to the nature of galvanic deposition and were therefore deemed undesirable. The formation of various trench depths was achieved by controlling the electrochemical etching duration, with a nearly constant etch rate displayed for both 0.025 and 0.1 μm thick sacrificial layers for all time periods <10 min. Bi_xTe_y nanoribbons were synthesized by galvanically displacing the exposed nickel (Fig. 1e) at room temperature. The displacement time was adjusted to control the width of the nanoribbons. After synthesis of the nanoribbons, the photoresist and nickel were selectively removed using acetone and 2% (v/v) nitric acid, respectively (Fig. 1g). Gold/chromium micro-electrodes were subsequently fabricated on top of the nanoribbons using a lift-off technique to investigate the composition and temperature dependent electron transport properties (Fig. 1h).

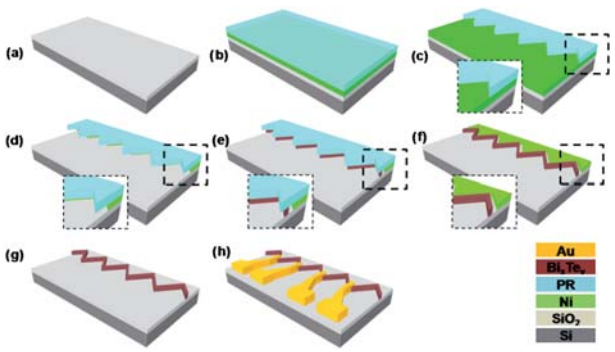

Fig. 1 Schematic illustrations of Bi_xTe_y nanoribbon synthesis by Lithographic Patterned Galvanic Displacement (LPGD): SiO_2 layer ($t_{ox} = 0.3$ μm) was deposited by atomic layer epitaxy followed by the photolithographic patterning of align marks (a). The sacrificial layer was e-beam evaporated on substrate followed by spin-coating of PR (b), PR was developed (c). The sacrificial layer was chemically or electrochemically etched to create the undercut trench (d). The nanoribbons were galvanically displaced using the vertical exposed layer as an electrode (e), followed by removal of PR (f) and the sacrificial layer (g). Cr and Au were e-beam deposited by the photolithographic patterning to form electrical contacts (h).

For TEM analysis, a focused ion beam (FIB) (NOVA 600 Nanolab, FEI) milling technique was utilized to dice small sections of the samples, followed by platinum deposition onto FIB-milled specimen in order to shield it from high energy associated with the ion beam in Fig. S2(a)†. The cross-sectional images of the FIB-milled Bi_xTe_y nanoribbons show the variation of nanoribbon thickness depending on the locations which might be attributed to reduction of trench gap due to bowing of photoresist (Fig. S2(c and d)†). Additionally, for the measurement of Seebeck coefficients, an e-beam lithographical patterning technique was utilized to create gold microheater and electrical contacts to as-synthesized 0.1 μm thick $Bi_{30}Te_{70}$ nanoribbons (Fig. 7a).

Results and discussion

Synthesis of the aligned Bi_xTe_y nanoribbons

Fig. 1 illustrates the detailed experimental procedure. The nickel sacrificial layers deposited on a silicon substrate were utilized to demonstrate control over the thickness of the nanoribbons. The lithographical patterned nickel layer was etched to impose a slight recess on the nickel nanoband. The exposed nickel in the trench is galvanically displaced by bismuth and tellurium ions in electrolytes, where the width of the nanoribbons depends on the displacement time. The electrolytes with different concentration of $HTeO_2^+$ and Bi^{3+} were used to investigate the effect of solution composition on nanoribbon content.[19–21] The difference in the redox potentials *i.e.* Ni^{2+}/Ni^0 ($E^0 = -0.257$ V *vs.* NHE) is more cathodic than Bi^{3+}/Bi^0 ($E^0 = 0.308$ V *vs.* NHE) and $HTeO_2^+/Te^0$ ($E^0 = 0.551$ V *vs.* NHE).[22,23] Since the Gibbs free energy of Bi_2Te_3 formation is negative (*i.e.* $\Delta G_f^0 = -899.088$ kJ mol^{-1}), the direct deposition of Bi_2Te_3 intermetallic compound is thermodynamically favorable over the codeposition of elemental Bi^0 and Te^0 metals,[24] which leads to the following reaction:

$$2Bi^{3+}(aq) + 3HTeO_2^+(aq) + 9Ni^0(s) + 9H^+(aq) \rightarrow Bi_2Te_3(s) + 9Ni_2^+(aq) + 6H_2O(aq) \quad (1)$$

Fig. 2 shows the complex shapes of the as-synthesized Bi_xTe_y nanoribbons (*i.e.* 0.1 μm thickness by 3 to 15.3 mm long). The geometrical layout and length of Bi_xTe_y nanowires were predetermined by the photolithographic mask. The thickness of Bi_xTe_y nanoribbons was dependent on the thickness of the sacrificial nickel layer. The width of synthesized Bi_xTe_y nanoribbons was monotonically increased with galvanic displacement reaction time at a fixed trench depth (Fig. 3).

The effects of trench dimensions (*i.e.* trench depth (up to 22 μm) and height (0.025 and 0.1 μm)) on the nanoribbon composition and deposition rate are shown in Fig. S1 of ESI†, where the nanoribbon compositions were measured using energy dispersive X-ray spectroscopy (EDS). As expected, the composition and

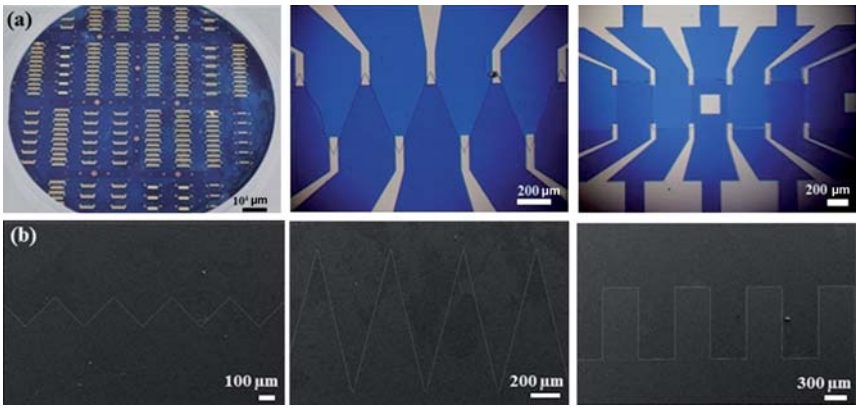

Fig. 2 Images of LPGA synthesized Bi_xTe_y nanoribbons in wafer-scale with different shapes: (a) optical images and (b) SEM images.

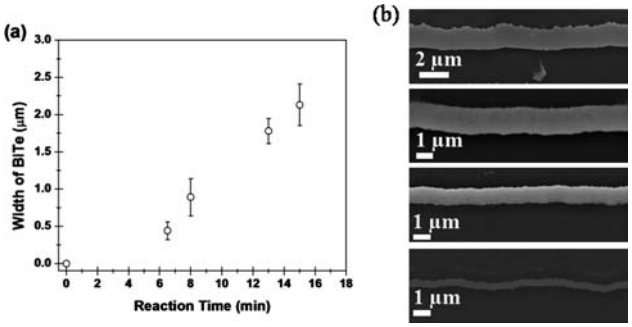

Fig. 3 (a) Width of Bi_xTe_y as a function of the deposition time and (b) SEM images of Bi_xTe_y nanoribbons with different widths. The electrolyte consisted of 4 mM Bi^{3+} and 10 mM $HTeO^+$ in 1 M HNO_3 at room temperature. The thickness of nickel was fixed at 0.1 μm. The trench depths were 13.6 ± 0.4 μm.

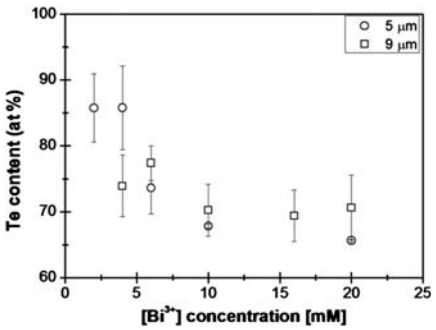

Fig. 4 Effect of the solution composition of deposited Te content. The Bi^{3+} concentration was varied from 2 mM to 20 mM while fixing the $HTeO^+$ concentration at 10 mM. The trench depth was varied from 5 to 9 μm. The thickness of nickel layer was fixed at 0.025 μm.

deposition rate were strongly dependent on the trench depth with the deposited Te content increasing and the deposition rate decreasing with increasing trench depth. Low deposition rates at greater trench depths might be attributed to slower diffusion rates of the metal ions within the trench. The nanoribbon composition was also dependent on the trench height resulting in a higher deposited Te content for the 0.025 μm thick trench than the 0.1 μm thick trench at a given trench depth. Higher Te content for deeper trenches with shorter height might be attributed to a faster deposition rate of Te(s) (eqn (2)) compared to UPD deposition of Bi to form Bi_2Te_3 (eqn (3)).

$$HTeO_2^+(aq) + 3H^+(aq) + 4e^- \rightarrow Te(s) + 2H_2O\ E^0 = +0.551\ V\ vs.\ NHE \quad (2)$$

$$3Te + 2Bi^{3+} + 6e^- \rightarrow Bi_2Te_3(s) \quad (3)$$

The effect of solution composition on the nanoribbons composition was investigated by varying Bi^{3+} concentration from 2 to 20 mM at a fixed concentration of $HTeO_2^+$ at 10 mM and trench depths of 5 and 9 μm (Fig. 4). Increasing the Bi^{3+} concentration enhanced the UPD deposition of Bi^{3+} on Te to form Bi_2Te_3 compounds (eqn (3)), which resulted in decreased Te content in the deposit. In addition, the deposition rate increased with increasing Bi^{3+} concentration (data not shown). These findings indicate that the dimension, composition, and deposition rate of Bi_xTe_y nanoribbons can be readily controlled by adjusting the deposition conditions.

To confirm the formation of Bi_2Te_3 intermetallic compound without the formation of Bi and Te elements, HR-TEM analysis with FFE-converted SAED patterns was performed. Prior to TEM analysis, approx. 0.025 μm thick $Bi_{31}Te_{69}$ and 0.1 μm thick $Bi_{29}Te_{71}$ nanoribbons were annealed at 200 °C for 8 hours in 5% H_2/N_2 environments to improve the crystallinity and reduce the defect sites. Fig. 5 shows the HR-TEM images with FFT-converted SAED patterns. Similar to the X-ray diffraction patterns[25] of galvanically displaced Bi_xTe_{1-x} thin films from the sacrificial nickel thin films, FFT-converted SAED patterns confirmed the formation of polycrystalline Bi_2Te_3 intermetallic compounds with a rhombohedral structure without elemental Te and Bi.[25] As shown in our prior work, elemental Te started to precipitate when the Te content is greater than 80 at%.[25] The lattice parameters of polycrystalline Bi_xTe_y nanoribbons differed by the converted location where the average lattice parameters of 0.1 μm thick $Bi_{31}Te_{69}$ nanoribbon were $a = 4.377$ (±0.22) Å and $c = 30.59$ (±0.39) Å and the average lattice parameters of 0.025 μm thick $Bi_{29}Te_{71}$ nanoribbon were $a = 4.360$ (±0.29) Å and $c = 30.70$ (±0.47) Å. Compared to bulk Bi_2Te_3 ($a = 4.359$ Å and $c = 30.44$ Å), they show a larger c-axis lattice parameter.[26–28] Since Te atoms are larger than the interstitial sites (*i.e.* octahedral

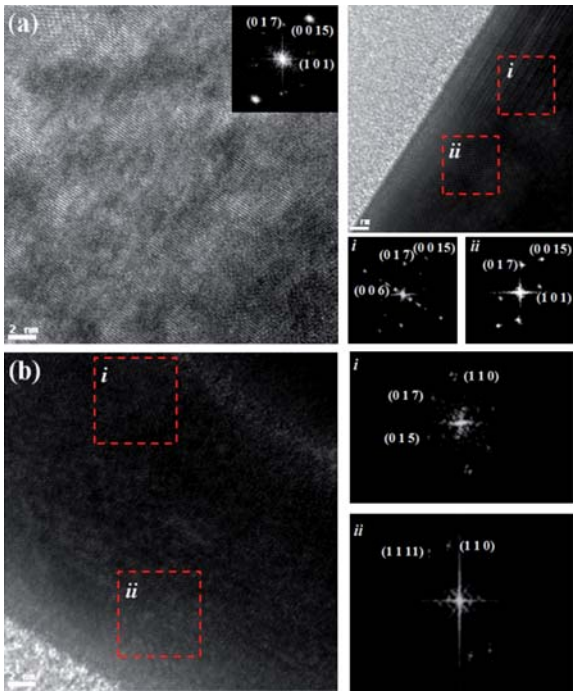

Fig. 5 High resolution TEM images and FFT-converted SAED patterns: (a) $Bi_{31}Te_{69}$ nanoribbon (0.1 × 0.77 micron) and (b) $Bi_{29}Te_{71}$ nanoribbon (0.025 × 0.89 micron) annealed at 200 °C for 8 h in 5% H_2/N_2 environment.

or tetragonal site) of Bi_2Te_3 compound and have high solubility,[29–31] it is expected that the excess Te atoms will occupy Bi lattice sites in the Bi_2Te_3 crystal structure which will alter the lattice parameters and will act as n-type dopants.

Electrical characteristics of the Bi_xTe_y nanoribbons

The electrical resistivity of Bi_xTe_y nanoribbons was measured using a 4-point probe contact method to eliminate the contact resistance. As listed in Table 1, the electrical resistivity of Bi_xTe_y nanoribbons was one to two orders of magnitude higher than single crystalline bulk and nanowire counterparts due to poor crystallinity and greater porosity which lead to higher defect scattering. Although the Seebeck coefficient of the nanoribbon was greater than counterparts, the power factor was lower due to

Table 1 Comparison of electrical resistivity (ρ), Seebeck coefficient (S), and power factor between nanoribbon, nanowire, and bulk counterpart

Structure	Composition	Temp/ K	Resistivity/ 10^{-6} Ω m	S/ μV K^{-1}	Power factor/ μW m^{-1} K^{-2}
Bulk[30]	$Bi_{29.5}Te_{70.5}$	300	2.6	−115	5090
Nanowire[31]	Te-rich BiTe	300	14.2	−30	63
Nanowire[32]	Bi-rich single crystalline $Bi_{74}Te_{26}$	300	4.6	−52	581
This work[a]	$Bi_{31}Te_{69}$	270	289	−180	110

[a] LPGD-synthesized $Bi_{31}Te_{69}$ nanoribbon with the cross-sectional area of 0.1 × 0.77 μm^2.

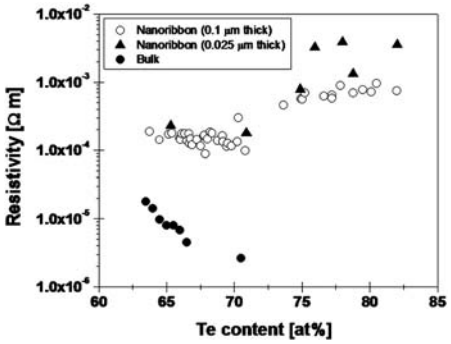

Fig. 6 Effect of the composition on the resistivity of the Bi_xTe_y nanoribbons: ρ *vs.* Te contents curve.

high electrical resistivity. To investigate the effect of thickness on the electrical properties of Bi_xTe_y nanoribbons, nanoribbons with two different thicknesses (*i.e.* 25 nm and 100 nm) were synthesized and their electrical properties were compared (Fig. 6). Compared to 100 nm thick nanoribbons, 25 nm thick nanoribbons showed higher electrical resistivity which indicated that reduction of thickness leads to greater surface boundary scattering. Additionally, we investigated the composition dependent electrical resistivity of Bi_xTe_y nanoribbons and compared them with bulk counterparts. Two distinct trends were observed where the electrical resistivity slightly decreased with increased Te content at the composition of 62 to 72 at% Te. When the deposited Te content is greater than 72 at%, the electrical resistivity increased with increased Te content. Bi_xTe_y has a rhombohedral crystal structure that belongs to the space group $D^5_{3d}(R\bar{3}m)$ having a unit cell with lattice constants a = 4.38 Å and c = 30.45 Å in a hexagonal representation. Excess Te in semiconducting Bi_xTe_y nanoribbons acts as an n-type dopant as well as a defect for charge carrier scattering because the excess Te occupies Bi lattice sites in the crystal structure.[27] At the deposited Te content from 62 to 72 at%, excess Te may increase carrier concentration which resulted in a decrease in electrical resistivity. When the composition of Bi_xTe_y nanoribbons deviated greatly from the stoichiometric Bi_2Te_3 compound, crystalline defects and a rough, porous microstructure may play a more critical role than dopant level. As shown in AFM images (Fig. S3†), Bi_xTe_y nanoribbons with higher Te contents (77.83 at% Te) show a more rough, porous morphology compared to nearly stoichiometric Bi_xTe_y nanoribbons (67.8 at% of Te). Nearly stoichiometric Bi_xTe_y nanowire (63.7 at% Te) showed that the arithmetic average of absolute roughness (R_a) was 2.5 × 10^{-3} μm. In contrast, the Bi_xTe_y nanoribbons with higher Te content (82.0 at% Te) had greater R_a of 5.5 × 10^{-3} μm (Fig. S3†).

Field effect transistor (FET) properties, such as the field effect carrier mobility, were measured to investigate the electronic transport properties of single Bi_xTe_y nanoribbons. The inset of Fig. S4a† shows the FET schematic diagram. Fig. S4a† shows typical transfer characteristics (I_{ds}–V_{gs}) of a Bi_xTe_y nanoribbon (69.5 at% of Te) at V_{ds} = +1 V with the width of 0.89 μm and length of 385 μm. The I_{ds} *versus* V_{gs} curve displayed n-type semiconductor behavior. According to previous studies of bulk Bi_xTe_y materials, these n-type characteristics could arise from the presence of Bi vacancies.[33] The field-effect carrier mobilities of

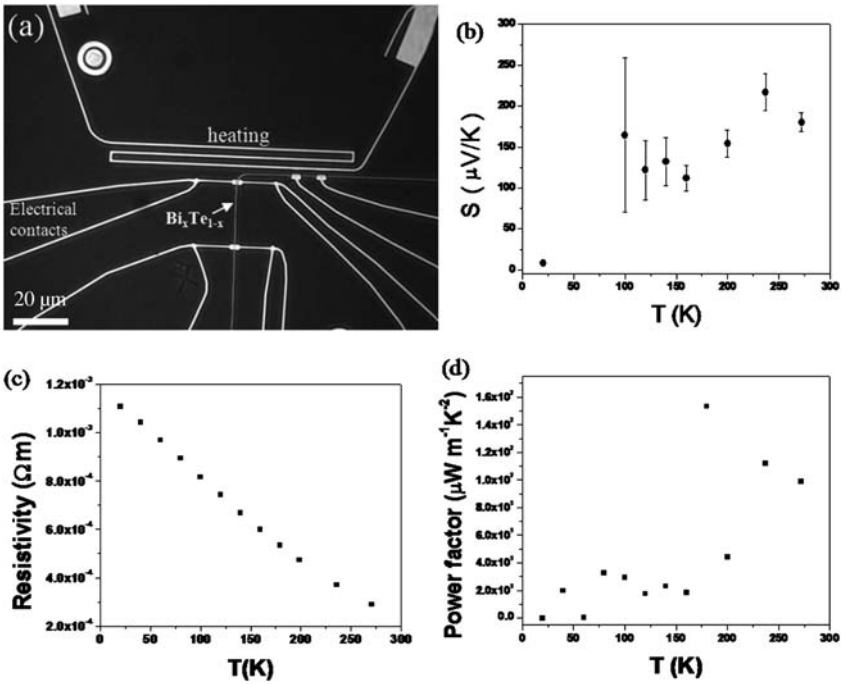

Fig. 7 SEM image of electrically connected $Bi_{30}Te_{70}$ nanoribbon (cross-sectional area of 0.1 × 0.77 μm^2) (a) and temperature dependent Seebeck coefficient (b), electrical resistivity (c), and power factor (d).

Bi_xTe_y nanowires ranged from 10–60 cm^2 V^{-1} s^{-1} independent of composition, which might be attributed to the trapped charges at the interface between a channel and dielectric layer (Fig. S4b†).[30]

The temperature dependent electrical resistivity of as-deposited and annealed Bi_xTe_y nanoribbons was investigated from 400 to 25 K (Fig. S5†). The annealing was performed in a reducing environment (5% H_2 + 95% N_2) at 473 K with an annealing time from 2 to 8 hours (Fig. S5†). The resistivity of n-type Bi_xTe_y decreased at high temperature due to a drastic increase in carrier concentration compared to the slow decrease of mobility with rising temperature. The annealing effects of Bi_xTe_y on resistivity showed that the carrier density decreased with increasing annealing time corresponding to that of a Bi_xTe_y thin film.[21,34] The thermal activation energies of the Bi_xTe_y nanoribbon before and after the annealing were calculated from the temperature dependence of resistivity. The activation energies for the Bi_xTe_y nanowire before and after the annealing process were 9.42 meV and 13.4 meV, respectively, which might be attributed to decrease in the defect level of Bi_xTe_y nanoribbons due to the improvement in crystallinity.

To determine some thermoelectric properties including electrical resistivity and Seebeck coefficient, e-beam lithographical patterning was utilized to create gold microheater and electrical contacts to as-synthesized 0.1 μm thick $Bi_{30}Te_{70}$ nanoribbons (Fig. 7a). A temperature gradient within the specimens was created by introducing electrical pulses on the microheaters. Fig. 7b and d show the temperature dependent electrical resistivity, Seebeck coefficient, and power factor, respectively. Compared to its bulk and nanowire counterpart, the Seebeck coefficient of the nanoribbon was slightly higher (Table 1). However, the power factor was one order of magnitude lower than bulk and nanowire counterparts.[31,32,35] By annealing the nanoribbons, we anticipate that the power factor can be further enhanced by improving crystallinity similar to thin films.[21]

Conclusions

We have demonstrated the wafer level batch synthesis and fabrication of single semiconducting nanoribbon based devices. The shape, dimension, and composition of nanoribbons were controlled by adjusting the electrolyte composition, deposition conditions, and thickness of the sacrificial layer. Composition dependent electrical resistivity shows two distinct regions, where Bi_xTe_y nanoribbons with Te content between 62 and 72 at% show increased electrical resistivity with increased Te content and where excess Te may increase carrier concentration to reduce electrical resistivity. When the composition of Bi_xTe_y nanoribbons deviated greatly from the stoichiometric Bi_2Te_3 compound (>72 at%) crystalline defects and a porous microstructure play a more critical role than dopant level, which resulted in increased electrical resistivity with increase in Te content. The as-synthesized Bi_xTe_y nanoribbons were n-type semiconductors. There were no clear trends between the field effect carrier mobilities and composition and dimensions which might be attributed to the trapped charges at interface between a channel and dielectric layer.

LPGD is a precise, reliable, and IC-compatible method to fabricate nanoscale electronic devices because it allows batch synthesis of high density complex shaped nanostructures with controlled dimensions and composition to predetermined location in a cost effective manner.

Acknowledgements

This work was supported by the Pioneer Research Center Program through National Research Foundation of Korea (2010-0002231) funded by the Ministry of Education, Science and Technology (MEST) and the Fundamental R&D program for Core Technology of Materials funded by the Ministry of Knowledge Economy (MKE), Republic of Korea.

References

1 Y. Cui and C. M. Lieber, *Science*, 2001, **291**, 851.
2 Y. Cui, Q. Wei, H. Park and C. M. Lieber, *Science*, 2001, **293**, 1289.
3 M. S. Gudiksen, L. J. Lauhon, J. Wang, D. C. Smith and C. M. Lieber, *Nature*, 2002, **415**, 617.
4 J.-i. Hahm and C. M. Lieber, *Nano Lett.*, 2004, **4**, 51.
5 Y. Huang, X. Duan, Y. Cui, L. J. Lauhon, K.-H. Kim and C. M. Lieber, *Science*, 2001, **294**, 1313.
6 M. H. R. Lankhorst, B. W. S. M. M. Ketelaars and R. A. M. Wolters, *Nat. Mater.*, 2005, **4**, 347.
7 L. J. Lauhon, M. S. Gudiksen, D. Wang and C. M. Lieber, *Nature*, 2002, **420**, 57.
8 B. Y. Yoo, F. Xiao, K. N. Bozhilov, J. Herman, M. A. Ryan and N. V. Myung, *Adv. Mater.*, 2007, **19**, 296.
9 D. Yu, S. Brittman, J. S. Lee, A. L. Falk and H. Park, *Nano Lett.*, 2008, **8**, 3429.
10 T. Zhang, S. Mubeen, N. V. Myung and M. A. Deshusses, *Nanotechnology*, 2008, **19**, 332001.
11 S. Donthu, Z. Pan, B. Myers, G. Shekhawat, N. Wu and V. Dravid, *Nano Lett.*, 2005, **5**, 1710.
12 K. Salaita, Y. Wang and C. A. Mirkin, *Nat. Nanotechnol.*, 2007, **2**, 145.
13 D. Natelson, *Nat. Mater.*, 2006, **5**, 853.
14 E. J. Menke, M. A. Thompson, C. Xiang, L. C. Yang and R. M. Penner, *Nat. Mater.*, 2006, **5**, 914.
15 Y. Yang, S. C. Kung, D. K. Taggart, C. Xiang, F. Yang, M. A. Brown, A. G. Güell, T. J. Kruse, J. C. Hemminger and R. M. Penner, *Nano Lett.*, 2008, **8**, 2447.
16 E. J. Menke, M. A. Brown, Q. Li, J. C. Hemminger and R. M. Penner, *Langmuir*, 2006, **22**, 10564.
17 R. Venkatasubramanian, T. Colpitts, E. Watko, M. Lamvik and N. El-Masry, *J. Cryst. Growth*, 1997, **170**, 817.
18 R. Venkatasubramanian, E. Siivola, T. Colpitts and B. O'Quinn, *Nature*, 2001, **413**, 597.
19 F. Xiao, B. Y. Yoo, K.-H. Lee and N. V. Myung, *J. Am. Chem. Soc.*, 2007, **129**, 10068.
20 F. Xiao, B. Y. Yoo, K.-H. Lee and N. V. Myung, *Nanotechnology*, 2007, **18**, 335203.
21 B. Y. Yoo, C. K. Huang, J. R. Lim, J. Herman, M. A. Ryan, J. P. Fleurial and N. V. Myung, *Electrochim. Acta*, 2005, **50**, 4371.
22 D. R. Lide, *CRC Handbook of Chemistry and Physics*, CRC Press, Cleveland, 2007–08.
23 F. Xiao, B. Y. Yoo, M. A. Ryan, K.-H. Lee and N. V. Myung, *Electrochim. Acta*, 2006, **52**, 1101.
24 M. S. Martin-Gonzalez, A. L. Prieto, R. Gronsky, T. Sands and A. M. Stacy, *J. Electrochem. Soc.*, 2002, **149**, C546.
25 C. H. Chang, Y. Rheem, Y. H. Choa, D. Y. Park and N. V. Myung, *Electrochim. Acta*, 2010, **55**, 1072.
26 J. O. Barnes, J. A. Rayne and R. W. Ure, *Phys. Lett. A*, 1973, **44**, 215.
27 S. Cho, Y. Kim, A. DiVenere, G. K. Wong, J. B. Ketterson and J. R. Meyer, *Appl. Phys. Lett.*, 1999, **75**, 1401.
28 Y. Kim, S. Cho, A. DiVenere, G. K. L. Wong and J. B. Ketterson, *Phys. Rev. B: Condens. Matter Mater. Phys.*, 2001, **63**, 155306.
29 H. A. Wriedt, N. A. Gokcen and R. H. Nafziger, *ASM Handbook*, ed. H. Baker, 2005, vol. 3.
30 A. Emrani, G. Ghibaudo, F. Balestra, B. Piot, V. Thirion and A. Straboni, *J. Appl. Phys.*, 1993, **73**, 5241.
31 J. Zhou, C. Jin, J. H. Seol, X. Li and L. Shi, in Thermoelectrics, 2005. ICT 2005. 24th International Conference on 2005, 17.
32 A. Mavrokefalos, A. L. Moore, M. T. Pettes, L. Shi, W. Wang and X. Li, *J. Appl. Phys.*, 2009, **105**, 104318.
33 J. P. Fleurial, L. Gailliard, R. Triboulet, H. Scherrer and S. Scherrer, *J. Phys. Chem. Solids*, 1988, **49**, 1237.
34 C. B. Satterthwaite and R. W. Ure, *Phys. Rev.*, 1957, **108**, 1164.
35 D. M. Rowe, *CRC Handbook of Thermoelectrics*, CRC Press Inc., Boca Raton, 1995.